

Fast acquisition of activation energy maps using temperature ramps for lifetime modeling of BTI

K. Puschkarsky^{1,2}, H. Reisinger¹, C. Schl nder¹, W. Gustin¹ and T. Grasser²

¹ Infineon Technologies AG, Am Campeon 1-15, D-85579 Munich, Germany

² Vienna University of Technology, Gu hausstr.25, AT-1030 Vienna, Austria

Abstract—Accelerating Bias Temperature Instability (BTI) through temperature activated charge trapping and chemical reactions is commonly used during qualification measurements of MOSFETs to enable lifetime extrapolation of typically up to ten years. Capture and emission time (CET) maps extracted from measurement data at constant temperatures are used to model the time dynamics responsible for the threshold voltage shift of BTI. We demonstrate a new measurement technique for the acquisition of CET maps and show that Arrhenius temperature activation is valid for a large number of defects and can be described by an activation energy map. The goal of the temperature accelerated MSM technique is to extend the experimental time window of degradation and recovery to more than 10 years without requiring voltage acceleration and time extrapolation.

Index Terms—CET, BTI, temperature acceleration.

I. INTRODUCTION

IN the past decades the negative bias temperature instability has been one of the most critical reliability issues for silicon-based MOSFETs [1]–[3]. The negative bias temperature instability can in good approximation be understood as the collective response of independent defects and the kinetics of the defects can be described by a capture and emission time constant for each individual defect [4], which correspond to the reciprocal rates of chemical reactions [5]. The investigation of the physical mechanisms of BTI requires stress and recovery times covering several decades in time (further called experimental window), limited by the measurement equipment ($\approx 1 \mu\text{s}$ measurement delay) and the measurement time available [6]. Numerous studies have shown that oxide and interface defects contribute to BTI. Furthermore, there is evidence, that oxide defects are mainly responsible for the recoverable component of BTI and interface defects are mostly permanent in typical experimental windows [7], [8]. The temperature dependence of the individual defect time constants is given by the Arrhenius law [9]:

$$\tau = \tau_0 \cdot \exp\left(\frac{E_a}{k_B T}\right) \quad (1)$$

with an activation energy E_a , Boltzmann's constant k_B and the time constant τ_0 . Pobegen et al. [10] have shown, for recovery and degradation independently, that this temperature dependence of the capture and emission time constants is also valid for a large ensemble of defects. Following equation 1 we can calculate the defect time constant change when changing the temperature. With this assumption and the identification of τ_0 data recorded at a reference temperature T_{ref} can be drawn as a function of the time equivalent to a temperature, called the temperature-time $\theta(T)$. A schematic for the temperature acceleration of defects within the experimental window is

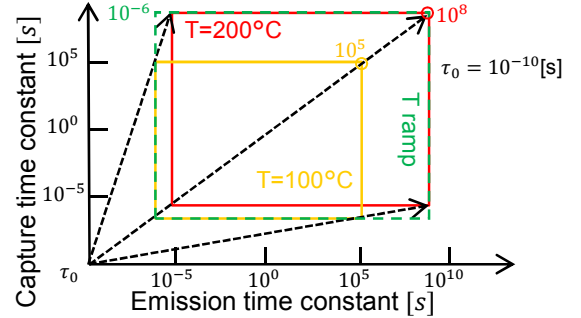


Fig. 1. **Arrhenius temperature activation:** The experimental window at $T=100^\circ\text{C}$ is shown in orange, with stress and recovery times up to 100 ks. Performing the same experiment at $T=200^\circ\text{C}$ shifts the long capture and emission time constants equivalent to $T=100^\circ\text{C}$ of up to 10 years into the measurement window. The most important drawback is that with a limiting measurement delay of $1 \mu\text{s}$, the shortest measurable equivalent capture and emission time constant at $T=200^\circ\text{C}$ is $20 \mu\text{s}$ (red lines). The new measurement technique (dashed green lines) overcomes this drawback and achieves measurement of the capture and emission time constants of $1 \mu\text{s}$ and with the temperature acceleration measurement of equivalent time constants of more than 10 years.

illustrated in Fig. 1. With recovery and stress times of $1 \mu\text{s}$ up to 100 ks at $T=200^\circ\text{C}$, the equivalent measurement window at $T=100^\circ\text{C}$ ranges from $20 \mu\text{s}$ up to 10 years. At $T=200^\circ\text{C}$ information from defects with equivalent capture and emission time constants below $20 \mu\text{s}$ at $T=100^\circ\text{C}$ is lost.

The measurement technique introduced in Chapter II, overcomes this drawback and achieves measurement of the capture and emission time constants of $1 \mu\text{s}$ while keeping the advantage of the temperature acceleration and reaching time constants equivalent to $T=100^\circ\text{C}$ of more than 10 years (dashed green lines). We will show in Chapter III for NBTI degradation and recovery, that also for devices with a large number of defects and widely distributed time constants, the temperature activation of capture and emission follows the Arrhenius law. The threshold voltage shift after NBTI stress and recovery at three different temperatures can be modeled with a single activation energy map using the Arrhenius temperature activation. In contrast to the work of Pobegen et al., we model both degradation and recovery simultaneously [10] and present an activation energy map. It includes the temperature dependence of the defect time constants for the recoverable component with the unique time constant $\tau_{0,r}$ and the permanent component with the unique time constant $\tau_{0,p}$. In Chapter IV, we present temperature accelerated MSM (TA-MSM) results enabling lifetime modeling of NBTI without the need of time extrapolation.

II. EXPERIMENTAL DETAILS

Samples used were pMOSFETs ($W=10\mu\text{m}$, $L=130\text{nm}$) from a 130 nm technology, with a 2.2nm nitrided gate oxide. The electrical measurements were done using our ultra-fast MSM measuring technique as described in [6]. Due to thermal expansion of components such a measurement is challenging to perform on wafer-level. Therefore an electric oven has been constructed to house the transistor (within the ceramic package) between two aluminum half shells. The temperature of the aluminum half shells is controlled and stabilized via a Pt-1000 thermometer, mica heaters and a PID-controller. Cooling is done with compressed, cooled air. To achieve an acceleration of the recovery and still being able to measure the capture and emission of defects with short emission times, linear temperature ramps are performed.

A major part of the accelerated recovery actually occurs during the up-ramps of the temperature (see Fig. 5). Thus the ΔV_{th} , the difference between a given recovery trace and the first, pre-stress reference trace, needs to be recorded during the up-ramps. This is necessary since V_{th} is a function of temperature and decreases with a rate of $0.96 \pm 0.05\text{ mV/K}$. As the error in the absolute value of the temperature is not relevant, an error below $\pm 1\text{ K}$ is fully sufficient, while a steady-state temperature stability of $\pm 1\text{ mK}$ is desirable. The measurement scheme for the accelerated acquisition of CET-maps is illustrated in Fig. 2. As explained in Fig. 1 the goal is to extend the experimental time window of degradation and recovery to more than 10 years. Simply increasing the temperature would accelerate both degradation and recovery; the experimental window in Fig. 1 would shift right/up; thus information about defects with short capture and emission time constants would be lost. This is why a more sophisticated scheme has been developed. Fig. 2a): For short stress times (below 1ms), both the stress and the recovery temperature remain constant. For medium stress times (below 10ks, Fig. 2b), the recovery temperature remains constant for the first 1000 s and is afterwards linearly increased by 100 K within 1000 s. Right before the next stress-recovery sequence, the sample is cooled down to the base temperature. To reduce the absolute stress time (Fig. 2c),

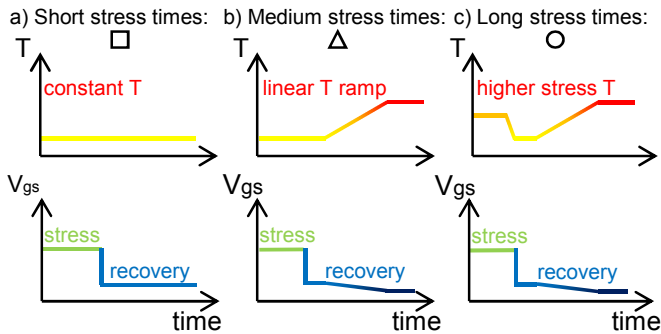


Fig. 2. Measurement scheme: **a) Short stress times:** Recovery and stress temperature is constant. **b) Medium stress times:** For the first 1000 s the recovery temperature is kept constant and is afterwards linearly increased by 100 K within 1000 s. V_{th} is a function of temperature and decreases during the temperature ramp. Right before the next stress sequence, the sample is cooled down. **c) Long stress times:** Increased stress temperature. After stress, the temperature is decreased to the recovery temperature keeping the stress voltage applied. The measurement scheme for the V_{th} recovery is the same as for medium stress times. The squares, triangles and circles indicate in Fig. 5 and 6, which measurement sequence has been applied.

the stress temperature is also increased. The temperature is decreased again after the stress to the base temperature keeping the stress voltage applied. The recovery temperature pattern is the same as for the medium stress times.

III. THE ACTIVATION ENERGY MAP

A wide range of experimentally observed features of NBTI can be explained in an analytical form using capture and emission time maps [11]. The analytic CET map model assumes, that the thermally activated charge exchange of independent defects leads to BTI. Charge exchange as well as first-order reactions creating interface states can be described consistently with previous work as two bivariate Gaussian distributions [4]. One bivariate Gaussian distribution models the oxide defects being mainly responsible for the recoverable component and the other defect distribution models the interface defects which are mostly permanent in typical experimental windows [7], [8]. The main parameters of the analytic model are the mean values of the capture and emission activation energies E_{ac} and E_{ae} (μ_c and μ_e) with their standard deviations (σ_c and σ_e). In addition, the emission activation energies (E_{ae}) increase with larger capture activation energies (E_{ac}): $E_{\text{ae}} = E_{\text{ac}} + \Delta E_{\text{ae}}$. The implicit correlation between the standard deviations $\sigma_e^2 = r\sigma_c^2 + \sigma_{\Delta_e}^2$ as explained in [12] is used, with the correlation parameter $r = 1$ for the recoverable component and $r = 0$ for the permanent component. Thus the charged trap density $g(E_c, E_e)$ with amplitudes A_r , A_p for each component is given by:

$$g(E_c, E_e) = \frac{A}{2\pi\sigma_c\sigma_{\Delta_e}} \cdot \exp\left(-\frac{(E_c - \mu_c)^2}{2\sigma_c^2} - \frac{(E_e - (rE_c + \mu_{\Delta_e}))^2}{2\sigma_{\Delta_e}^2}\right). \quad (2)$$

The integral of the activation energy map over all defects being charged up to the stress time t_s ($\tau_c < t_s$) and not yet being discharged at the recovery time t_r ($\tau_e > t_r$) gives the threshold voltage shift. The activation energy map is a temperature-independent map and the capture and emission time maps at constant temperature result using equation 1 with one characteristic temperature-independent constant $\tau_{0,r}$ for the recoverable and $\tau_{0,p}$ for the permanent defects [10].

IV. MSM MEASUREMENTS AT CONSTANT TEMPERATURE

The recovery of the threshold voltage shift ΔV_{th} after different stress times at three different temperatures $T=100^\circ\text{C}$, $T=150^\circ\text{C}$, $T=200^\circ\text{C}$ is shown in Fig. 3. The acceleration of NBTI by higher temperatures is clearly visible as increased ΔV_{th} . The comparison of the ΔV_{th} described by the analytic CET map model (marked as solid lines in Fig. 3) with the experimental data of the three temperatures shows excellent agreement for all temperatures, stress and recovery times. The dashed lines correspond to the contribution of only the permanent component. In Fig. 4a), the activation energy map with the normalized defect density is shown in dependence of the capture and emission activation energies. The distribution of the permanent component, shown in Fig. 4d), is located at high capture activation energies and increasing emission activation energies, whereas the recoverable defects, shown in Fig. 4c), have smaller capture as well as smaller emission activation energies. Fitting the experimental data, we obtain the

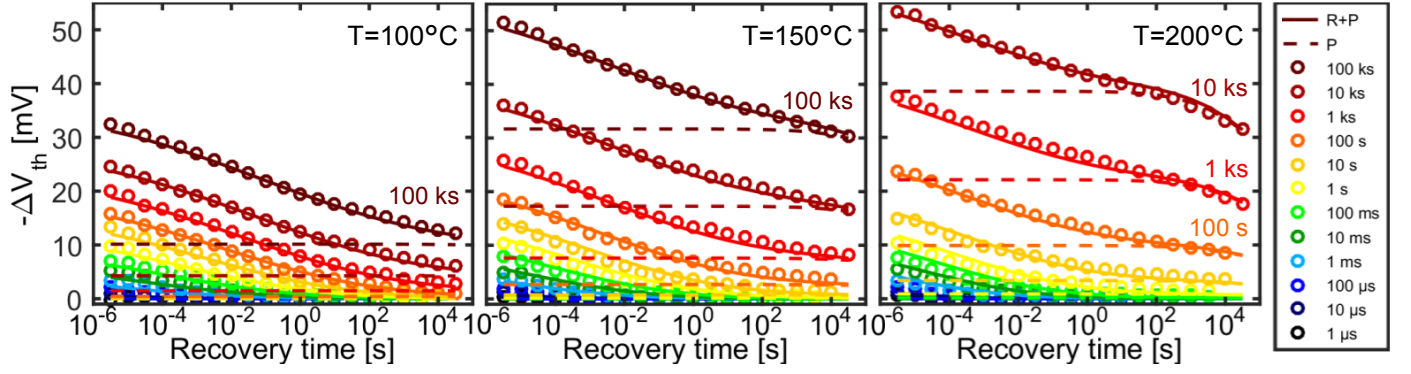


Fig. 3. MSM sequences at $T=100/150/200^\circ\text{C}$ with $V_{\text{gs}} = -2\text{V}$, $V_{\text{rec}} = -0.3\text{V}$ for stress times of $1\mu\text{s}$ to 100ks . The common activation energy map shown in Fig. 4 is used for the analytic model of all measurements. The comparison of the experimental data (circles) with the analytic model shows excellent agreement (solid lines: the sum of the recoverable and permanent component and the dashed lines: the contribution of only the permanent component).

characteristic temperature-independent constant $\tau_{0,r} = 55\text{fs}$ for the recoverable and $\tau_{0,p} = 0.57\text{ns}$ for the permanent component. The squares in Fig. 4a) mark the measurement windows in the energy space of the MSM measurements of Fig. 3. An activation energy of 1.6eV corresponds to an emission time constant of 100ks at $T=200^\circ\text{C}$ which is equivalent to 10^8s at $T=100^\circ\text{C}$. This enables modeling 10 years of NBTI stress and recovery based on measurement data without lifetime and voltage extrapolation. In Fig. 4b) the defect density of the capture and emission times at $T=100^\circ\text{C}$ is shown (calculated with $\tau = \tau_{0,p}$). With the constant temperature measurements, we have shown that the Arrhenius law for the change of the defect time constants with temperature can be considered together for stress and recovery using a unified activation energy map with temperature-independent time constants $\tau_{0,r}$ and $\tau_{0,p}$ for the recoverable and permanent component.

V. TEMPERATURE ACCELERATED MSM MEASUREMENTS

Performing several measurements at constant temperature is time and test device consuming. Therefore temperature accelerated measurements (TA-MSM) are performed (see Fig. 2) at a base stress temperature of $T=100^\circ\text{C}$ followed by a linear temperature ramp from $100 - 200^\circ\text{C}$. The stress temperature is increased for stress times larger than 10ks up to $T=190^\circ\text{C}$. The accelerated NBTI measurement results at constant stress voltage are shown in Fig. 5. Within the temperature ramp a huge acceleration of the recovery is visible (highlighted area in Fig. 5). Fig. 6 shows the same data set as in Fig. 5, but with the equivalent recovery time $\Theta(100^\circ\text{C})$ calculated using the Arrhenius law (see equation 1) with $\tau_0 = \tau_{0,p} = 0.57\text{ns}$, $T_1=100^\circ\text{C}$ and $T_2=T_{\text{meas}}$ for the change in temperature. The measurement data is displayed as open circles in Fig. 6. The huge acceleration of the recovery seen in Fig. 5 is stretched in time due to the time transformation with the Arrhenius law. As can be seen, the degradation is continuously recovering without a change of slope. The comparison of the measurement results and the analytic model shows a very good agreement in the extremely wide time window of up to 10 years equivalent time $\theta(T = 100^\circ\text{C})$. The activation energy map shown in Fig. 4, is obtained from the accelerated MSM measurements with continuous temperature change describing all stress/recovery and temperature dependencies of the measurements shown in Fig. 5. In addition

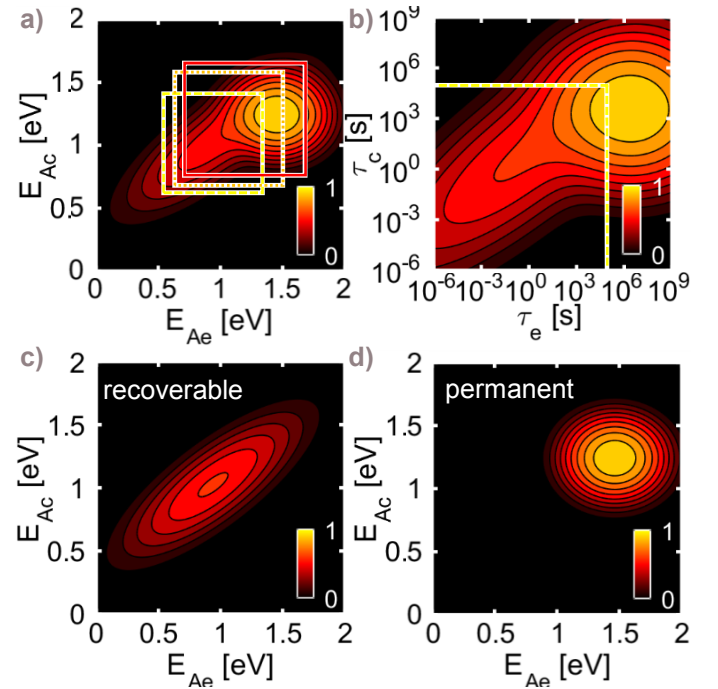


Fig. 4. **a)** The activation energy map extracted from the data of Fig. 5 ($V_{\text{gs}} = -2\text{V}$) containing all temperature dependent information. The threshold voltage shift obtained from this activation energy map is also a good fit to the data shown in Fig. 3. All maps are normalized using $\log_{10}(1 + \kappa \cdot g_{\text{max}})/\log_{10}(1 + \kappa)$, with g_{max} the maximum of the defect density of the sum of the recoverable and permanent component with $\kappa = 100$ to emphasize all details [11]. The squares show the experimental windows from the MSM measurements of Fig. 3 (yellow= 100°C , orange= 150°C , red= 200°C). **b)** The capture and emission time map calculated from a) at $T=100^\circ\text{C}$, with the yellow square marking the actual measurement window. **c)** The activation energy map, showing only the capture and emission activation energies of the recoverable component, whereas in **d)** the distribution of the activation energies of the permanent component are shown.

to describing the accelerated data, our model also provides a good description for the MSM measurements at constant temperature shown in Fig. 3. Due to the linear temperature ramp, not only discrete temperatures are included in the model. The continuous change in temperature during the recovery increases the model accuracy (least square optimum) by a factor of two for all measurements compared to the map obtained using only the constant temperature measurements.

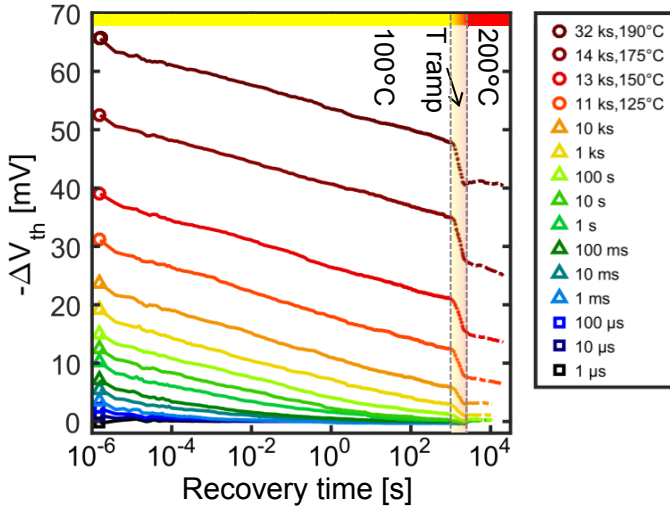


Fig. 5. Accelerated MSM measurement with $V_{gs} = -2$ V, base temperature $T=100^\circ\text{C}$. The ΔV_{th} is obtained subtracting the reference (including the temperature ramp) recorded before the stress from the measurement data. The squares, triangles and circles correspond to the measurement scheme shown in Fig. 2 a)-c), respectively. Measurements with stress times longer than 1 ms start with recovery at $T=100^\circ\text{C}$ of 100 s, followed by a linear temperature ramp within 1000 s from $100-200^\circ\text{C}$ and further recovery of up to 20 ks at $T=200^\circ\text{C}$. For the stress times up to 10 ks, the stress temperature is $T=100^\circ\text{C}$. The stress temperature is increased for stress times larger than 10 ks up to $T=190^\circ\text{C}$.

With the TA-MSM technique, only one measurement has to be performed per stress/recovery voltage, which speeds up measurement time by at least a factor of 10 to obtain the same measurement window with MSM measurements at three constant temperatures.

VI. CONCLUSIONS

For the first time, temperature acceleration of NBTI for stress and recovery have been considered together leading to a unified activation energy map with the characteristic temperature-independent constants for the recoverable and permanent component. In this paper, we demonstrated a new measurement technique using temperature ramps. For the TA-MSM technique no resistive heater structures are needed [13], [14] and the number of samples and the measurement time compared to MSM measurements at constant temperatures can be significantly reduced. Furthermore, this approach makes it possible to study many samples at the same stress conditions obtaining information about the degradation induced variability over the transistor lifetime without gate voltage acceleration and time extrapolation. In addition, the TA-MSM technique provides an implicit check for the assumption of Arrhenius activated individual traps. The application of the presented technique can be used to study the permanent component of NBTI and the recently discovered reverse recovery effect [15].

REFERENCES

- [1] J. Campbell; M. Lenahan; C. Cochrane; A. Krishnan and S. Krishnan; *Atomic-Scale Defects Involved in the Negative-Bias Temperature Instability*, IEEE Trans. Device Mater. Reliab. 7 (4), pp. 540-557, 2007.
- [2] V. Huard, M. Denais and C. Parthasarathy, *NBTI degradation: From physical mechanisms to modelling*, Microel. Rel. 46 (1), pp. 1-23, 2006.
- [3] M. Denais; V. Huard; C. Parthasarathy; G. Ribes; F. Perrier; N. Revil; A. Bravaix; *Interface Trap Generation and Hole Trapping Under NBTI and PBTI in Advanced CMOS Technology With a 2-nm Gate Oxide*, IEEE Trans. Device Mater. Reliab. 4 (4), pp. 715-722, 2004.

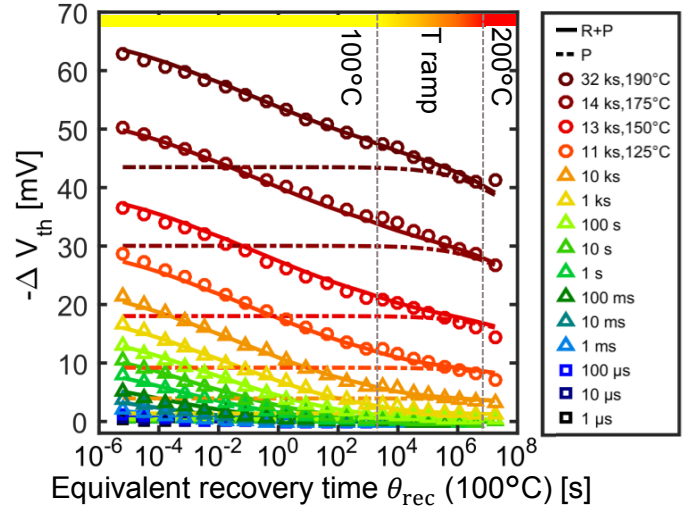


Fig. 6. Linearly interpolated measurement data (squares, triangles and circles) shown in Fig. 5, but with the calculated equivalent recovery times at $T_1=100^\circ\text{C}$ using the Arrhenius law (see equation 1) with $\tau_0 = \tau_{0,p} = 0.57$ ns and $T_2=T_{meas}$ for every change in temperature. The squares, triangles and circles correspond to the measurement scheme shown in Fig. 2 a)-c), respectively. The vertical grey dashed lines mark the area of the temperature ramp. The analytic model fit for the recoverable and permanent component, obtained from the activation energy map, is shown as solid lines, the dashed lines correspond to the contribution of only the permanent component.

- [4] T. Grassler, *Stochastic charge trapping in oxides: From random telegraph noise to bias temperature instabilities*, Microel. Rel. 52 (1), pp. 39-70, 2012.
- [5] B. Kaczer, T. Grassler, J. Martin-Martinez, E. Simoen, M. Aoulaiche, P. Roussel and G. Groeseneken; *NBTI from the perspective of defect states with widely distributed time scales*, in Proc.Intl. Rel.Phys.Symp. (IRPS), 2009, 44, pp. 55-60.
- [6] H. Reisinger; O. Blank; W. Heinrigs; A. Muhlhoff; W. Gustin; and C. Schlunder, *Analysis of NBTI degradation- and recovery-behavior based on ultra fast Vt-measurements*, in Proc.Intl.Rel.Phys.Symp. (IRPS), 2006, pp. 448-453.
- [7] V. Huard; *Two independent components modeling for Negative Bias Temperature Instability*, in Proc.Intl.Rel.Phys.Symp. (IRPS), 2010, pp. 2A.4-2A.4.10.
- [8] M. Alam; S. Mahapatra; *A comprehensive model of PMOS NBTI degradation*, Microelectronics Rel. 45 (1), pp. 71-81, 2005.
- [9] T. Grassler; H. Reisinger; P. Wagner; F. Schanovsky; W. Goes and B. Kaczer *The time dependent defect spectroscopy (TDDS) for the characterization of the bias temperature instability*, in Proc.Intl.Rel.Phys.Symp. (IRPS), 2010, pp. 16-25.
- [10] G. Pobegen and T. Grassler, *On the distribution of NBTI time constants on a long, temperature-accelerated time scale*, IEEE Trans. Electron Devices 60 (7), pp. 2248-2155, 2013.
- [11] T. Grassler, *Analytic modeling of the bias temperature instability using capture/emission time maps*, Electron Devices Meeting IEDM 2011, pp. 27.4.1-27.4.4.
- [12] Y. Illarionov, A. Smith, S. Vaziri, M. Ostling, T. Mueller, M. Lemme and T. Grassler; *Hot-carrier degradation and bias-temperature instability of single-layer graphene field-effect transistors*, in IEEE Transactions on electron devices, 2015, 62 (11), p.3876-3881.
- [13] T. Aichinger, M. Nelhiebel, S. Einspieler, T. Grassler; *In Situ Poly Heater - A Reliable tool for performing fast and defined temperature switches on chip*, Device and Materials Rel., Transactions on Electron Device Letters, 2010, 10, pp. 3-8.
- [14] G. Pobegen, M. Nelhiebel, S. de Filippis, T. Grassler; *Accurate high temperature measurements using local polysilicon heater structures*, Device and Materials Rel., Transactions on Electron Device Letters, 2014, 14, pp. 169-176.
- [15] T. Grassler, M. Walzl, K. Puschkarsky, B. Stampfer, G. Rzepa, G. Pobegen, H. Reisinger, H. Arimura and B. Kaczer; *Implications of gate-sided hydrogen release for post-stress degradation build-up after BTI stress*, in Proc.Intl. Rel.Phys.Symp. (IRPS), 2017.